Geodesy and Geodynamics 14 (2023) 485–499

Contents lists available at ScienceDirect

Geodesy and Geodynamics

journal homepage: http://www.keaipublishing.com/geog

Joint inversion of gravity and vertical gradient data based on modified structural similarity index for the structural and petrophysical consistency constraint

Sheng Liu [a, b, *], Xiangyun Wan [a], Shuanggen Jin [c, d, *], Bin Jia [a], Quan Lou [a], Songbai Xuan [d], Binbin Qin [a], Yiju Tang [a], Dali Sun [e]

[a] Henan University of Urban Construction, Pingdingshan 467041, China
[b] Institute of Geophysics, China Earthquake Administration, Beijing 100080, China
[c] School of Surveying and Land Information Engineering, Henan Polytechnic University, Jiaozuo 454000, China
[d] Shanghai Astronomical Observatory, Chinese Academy of Sciences, Shanghai 200030, China
[e] The First Monitoring and Application Center, CEA, Tianjin 300180, China

ARTICLE INFO

Article history:
Received 8 September 2022
Accepted 20 February 2023
Available online 29 March 2023

Keywords:
Joint inversion
Gravity and vertical gradient data
Modified structural similarity index

ABSTRACT

Joint inversion is one of the most effective methods for reducing non-uniqueness for geophysical inversion. The current joint inversion methods can be divided into the structural consistency constraint and petrophysical consistency constraint methods, which are mutually independent. Currently, there is a need for joint inversion methods that can comprehensively consider the structural consistency constraints and petrophysical consistency constraints. This paper develops the structural similarity index (SSIM) as a new structural and petrophysical consistency constraint for the joint inversion of gravity and vertical gradient data. The SSIM constraint is in the form of a fraction, which may have analytical singularities. Therefore, converting the fractional form to the subtractive form can solve the problem of analytic singularity and finally form a modified structural consistency index of the joint inversion, which enhances the stability of the SSIM constraint applied to the joint inversion. Compared to the reconstructed results from the cross-gradient inversion, the proposed method presents good performance and stability. The SSIM algorithm is a new joint inversion method for petrophysical and structural constraints. It can promote the consistency of the recovered models from the distribution and the structure of the physical property values. Then, applications to synthetic data illustrate that the algorithm proposed in this paper can well process the synthetic data and acquire good reconstructed results.

1. Introduction

Underground physical property models can be derived from the observed geophysical data using the geophysical inversion. However, the inherent multiple solutions remain challenges for the geophysical inversion. A variety of prior information for constraining the inversion [1–3] and the multiple geophysical data for the joint inversion [4–10] are both effective strategies to improve the non-uniqueness of the geophysical inversion.

There are two categories for the geophysical joint inversion methods according to whether the geophysical models recovered by the joint inversion of multiple geophysical data are the same. The first type is the joint inversion of the multiple geophysical data corresponding to the same physical property model, such as a

* Corresponding author. Henan University of Urban Construction, Pingdingshan 467041, China.
E-mail addresses: 1500240410@qq.com (S. Liu), xywan51@126.com (X. Wan), sgjin@shao.ac.cn (S. Jin), jia_yang1101@163.com (B. Jia), 20191009@hncj.edu.cn (Q. Lou), sbxuan@shao.ac.cn (S. Xuan), qinbinlj@126.com (B. Qin), tyj125@126.com (Y. Tang), 574111077@qq.com (D. Sun).

Peer review under responsibility of Institute of Seismology, China Earthquake Administration.

Production and Hosting by Elsevier on behalf of KeAi

https://doi.org/10.1016/j.geog.2023.02.004
1674-9847/

density model obtained from the joint inversion of gravity and gravity gradient data [11–16], a velocity model acquired by the joint inversion of first-arrival longitudinal wave and Rayleigh wave data [17] and a resistivity model recovered by the joint inversion of DC and electromagnetic data [18].

The second type is the geophysical data corresponding to the different physical property models. Additionally, these joint inversion methods are based on whether there are experimental or statistical relationships between the different physical property models. For example, a certain experimental empirical relationship between the seismic velocity and the gravity-derived density models can be utilized to execute the joint inversion for reducing the multiple solutions [19,20]. Additionally, the statistical relationships between density and susceptibility models obtained from the priori information of physical properties are applied to the joint inversion based on fuzzy C-means clustering algorithm [21,22]. Currently, a variety of geophysical joint inversion methods have been developed based on the structural consistency constraints, such as the cross-gradient constraint [23–27], the correlation constraint [28–32] and the Gramian constraint [33–35]. Additionally, some joint inversion methods based on field multi-component data or multidimensional data and the cross-gradient constraint under the condition of homologous problem are developed [36–38], which can significantly improve the multiplicity of solutions of the recovered models.

Currently, there is little research on the joint inversion method using structural constraints and petrophysical constraints. In this paper, we mainly focus on developing a new joint inversion method based on the structural consistency and petrophysical consistency to further improve the accuracy of inversion. Generally, in terms of images processing, the SSIM algorithm is a quantity for evaluation of the degree of the structural similarity of the different images. It comprehensively measures the similarity of the images from three aspects, images brightness contrast function, contrast function and structure contrast function [39]. Additionally, the brightness contrast function is based on the average of the images' pixels, the contrast function is based on the variance of the images' pixels, and the structure contrast function is based on the distribution structure of the images' pixels. The SSIM algorithm is a comprehensive measure of the images' consistency from the distribution characteristics of the different images' pixels values and the structure of the images' pixels distribution.

For the homologous problem of the geophysical inversion, the physical property models corresponding to the different component data are consistent in theory. However, the multiple solutions cover some differences in the physical property models acquired by the different component data. It can be considered that it is reasonable to constrain the structural consistency and petrophysical consistency from the perspectives of the similar structure and the similar petrophysical properties of the different recovered models. Therefore, the different physical-property models can be regarded as different images. The SSIM algorithm can be utilized as the structural and petrophysical consistency constraint to constrain the physical property models acquired by the inversion to reduce the non-uniqueness.

For the field data inversion, gravity gradient data has a high horizontal resolution and can highlight shallow geological bodies relative to the original gravity field. To adequately use the sensitivity difference between the gravity and gravity gradient data to the underground density structure, a joint inversion method based on the improved SSIM algorithm for the gravity and vertical gradient data is developed. In the actual application, the fractional form of the SSIM algorithm is transformed into the subtractive form, which can improve the problem of analytical singularities in the denominator and enhance the stability of the SSIM joint inversion method. Additionally, the reconstructed results are jointly constrained from the brightness, contrast and structural similarity of the density models corresponding to the gravity and vertical gradient data, respectively. Furthermore, the joint inversion is constrained by the weight functions obtained from the separate inverted results of the gravity and gravity gradient data [36]. Finally, the experiments on the synthetic data are adopted to certify that the resolution and accuracy of the reconstructed models obtained from the SSIM inversion are better than those acquired by traditional joint inversion.

2. Methodology

2.1. Modified structural similarity index

The density model is the physical property model corresponding to the gravity and vertical gradient data. Suppose that the density model $\boldsymbol{m}_1$ is recovered by the gravity data and the density model $\boldsymbol{m}_2$ is reconstructed by the vertical gradient data. Due to the multiplicity of the reconstructed models, there covers some inconsistency between the two density models. According to the structural similarity-evaluation algorithm [39,40], the SSIM algorithm between $\boldsymbol{m}_1$ and $\boldsymbol{m}_2$ can be expressed as the following equation.

$$\mathrm{SSIM}(\boldsymbol{m}_1,\boldsymbol{m}_2)=[L(\boldsymbol{m}_1,\boldsymbol{m}_2)]^{\alpha}[C(\boldsymbol{m}_1,\boldsymbol{m}_2)]^{\beta}[S(\boldsymbol{m}_1,\boldsymbol{m}_2)]^{\gamma}, \tag{1}$$

where $L(\boldsymbol{m}_1,\boldsymbol{m}_2)$ represents the brightness contrast function, $C(\boldsymbol{m}_1,\boldsymbol{m}_2)$ represents the contrast function and $S(\boldsymbol{m}_1,\boldsymbol{m}_2)$ represents the structure comparison function. α, β and γ represent the corresponding parameters of the above functions. The equationof the brightness contrast function, the contrast function and the structure comparison function have the following forms.

$$\begin{cases} L(\boldsymbol{m}_1,\boldsymbol{m}_2)=\dfrac{2\mu_{\boldsymbol{m}_1}\mu_{\boldsymbol{m}_2}+C_1}{\mu_{\boldsymbol{m}_1}^2+\mu_{\boldsymbol{m}_2}^2+C_1} \\ C(\boldsymbol{m}_1,\boldsymbol{m}_2)=\dfrac{2\sigma_{\boldsymbol{m}_1}\sigma_{\boldsymbol{m}_2}+C_2}{\sigma_{\boldsymbol{m}_1}^2+\sigma_{\boldsymbol{m}_2}^2+C_2} \\ S(\boldsymbol{m}_1,\boldsymbol{m}_2)=\dfrac{\sigma_{\boldsymbol{m}_1\boldsymbol{m}_2}+C_3}{\sigma_{\boldsymbol{m}_1}\sigma_{\boldsymbol{m}_2}+C_3} \end{cases}, \tag{2}$$

where $\mu_{\boldsymbol{m}_1}$ and $\mu_{\boldsymbol{m}_2}$ represent the mean values of $\boldsymbol{m}_1$ and $\boldsymbol{m}_2$, $\sigma_{\boldsymbol{m}_1}$ and $\sigma_{\boldsymbol{m}_2}$ represent the variances of $\boldsymbol{m}_1$ and $\boldsymbol{m}_2$, $\sigma_{\boldsymbol{m}_1\boldsymbol{m}_2}$ represents the covariance of $\boldsymbol{m}_1$ and $\boldsymbol{m}_2$, and C_1, C_2 and C_3 represent non-negative constant values. As the similarity of the different property models becomes stronger, the SSIM approaches to 1 or −1. When $\boldsymbol{m}_1$ and $\boldsymbol{m}_2$ are not similar, the SSIM term is equal to 0. The calculation equations of the mean, variance and covariance for the $\boldsymbol{m}_1$ can be expressed as the following equations.

$$\begin{cases} \mu_{\boldsymbol{m}_1}=\dfrac{1}{N}\displaystyle\sum_{i=1}^{N}\boldsymbol{m}_{1i} \\ \sigma_{\boldsymbol{m}_1}=\dfrac{1}{N-1}\displaystyle\sum_{i=1}^{N}(\boldsymbol{m}_{1i}-\mu_{\boldsymbol{m}_1}) \\ \sigma_{\boldsymbol{m}_1\boldsymbol{m}_2}=\dfrac{1}{N-1}\displaystyle\sum_{i=1}^{N}(\boldsymbol{m}_{1i}-\mu_{\boldsymbol{m}_1})(\boldsymbol{m}_{2i}-\mu_{\boldsymbol{m}_2}) \end{cases}, \tag{3}$$

where N is the number of meshing units. From Eqs. (1)–(3), when the SSIM algorithm is adopted to the inversion, it has the effect of constraining the inversion from the distributed characteristics'

similarity of density models' values and the distributed structures' similarity of the density models.

Because of the complexity of the underground geological conditions, there may be some parts of $\boldsymbol{m}_1$ and $\boldsymbol{m}_2$ that may be positively correlated, and some parts may be negatively correlated, causing these two parts to become uncorrelated when the correlations of these two parts are added together. Therefore, the processing methods of $\boldsymbol{x} = \boldsymbol{m}_1^2$ and $\boldsymbol{y} = \boldsymbol{m}_2^2$ are adopted to ensure that it is relevant in the above-mentioned situations [31]. Then, Eq. (1) can be transformed into the following equation.

$$\mathrm{SSIM}(\boldsymbol{x},\boldsymbol{y}) = [L(\boldsymbol{x},\boldsymbol{y})]^{\alpha}[C(\boldsymbol{x},\boldsymbol{y})]^{\beta}[S(\boldsymbol{x},\boldsymbol{y})]^{\gamma} \tag{4}$$

Let α, β and γ equal to 1, C_3=$C_2/2$, and C_1 is a constant value. Eq. (4) can be further transformed into the following equation.

$$\mathrm{SSIM}(\boldsymbol{x},\boldsymbol{y}) = \frac{\left(2\mu_{\boldsymbol{x}}\mu_{\boldsymbol{y}} + C_1\right)(2\sigma_{\boldsymbol{xy}} + C_2)}{\left(\mu_{\boldsymbol{x}}^2 + \mu_{\boldsymbol{y}}^2 + C_1\right)\left(\sigma_{\boldsymbol{x}}^2 + \sigma_{\boldsymbol{y}}^2 + C_2\right)} \tag{5}$$

In Eq. (5), the $\frac{1}{N}$ and $\frac{1}{N-1}$ in the calculation equations of the mean, variance and covariance in Eq. (3) are eliminated and those constants can also be eliminated in the following equations. To ensure the non-negativity and convenience of the calculation of the SSIM, C_1 and C_2 are set to zero and Eq. (5) can be transformed into the following equation.

$$\mathrm{SSIM}(\boldsymbol{x},\boldsymbol{y}) = \left(\mu_{\boldsymbol{x}}^2 + \mu_{\boldsymbol{y}}^2\right)\left(\sigma_{\boldsymbol{x}}^2 + \sigma_{\boldsymbol{y}}^2\right) \pm 4\mu_{\boldsymbol{x}}\mu_{\boldsymbol{y}}\sigma_{\boldsymbol{xy}} \tag{6}$$

From Eq. (6), when the similarity of the two physical property models is higher, the SSIM value will be smaller. However, Eq. (6) has the problem of choosing the signs, which is that the values of $\sigma_{\boldsymbol{xy}}$ for different parts of the physical property models may be positive or negative. For the convenience of the inversion, the following SSIM constraint can be obtained from Eq. (6).

$$\Phi_{\mathrm{SSIM}}(\boldsymbol{x},\boldsymbol{y}) = \left[\left(\mu_{\boldsymbol{x}}^2 + \mu_{\boldsymbol{y}}^2\right)\left(\sigma_{\boldsymbol{x}}^2 + \sigma_{\boldsymbol{y}}^2\right)\right]^2 - \left(4\mu_{\boldsymbol{x}}\mu_{\boldsymbol{y}}\sigma_{\boldsymbol{xy}}\right)^2 \tag{7}$$

Because of $\mu_{\boldsymbol{x}}^2 + \mu_{\boldsymbol{y}}^2 \geq 2\mu_{\boldsymbol{x}}\mu_{\boldsymbol{y}}$ and $\sigma_{\boldsymbol{x}}^2 + \sigma_{\boldsymbol{y}}^2 \geq 2\sigma_{\boldsymbol{xy}}$, the above transformation guarantees the non-negativity of the value of Eq. (7) and avoids the choice of the positive and negative signs. From Eq. (7), when the similarity of the physical property models is higher, the value of the SSIM constraint changes smaller. Additionally, from Zhdanov et al., 2012, the method proposed in this paper is based on the similarity of different physical property models, which can be considered as a form of the Gramian constraint. The difference between the two methods is that the means proposed in this paper is developed by digital image processing methods.

2.2. Objective function of the joint inversion

Eq. (7) is imposed on the objective function of the separate inversions for the gravity and vertical gradient data, respectively, and then the objective function of the SSIM joint inversion can be transformed into the following equations.

$$\begin{cases} \Phi_1 = \|\boldsymbol{d}_1 - \boldsymbol{G}_1\boldsymbol{m}_1\|_2^2 + \lambda_1\|\boldsymbol{w}_1\boldsymbol{m}_1\|_2^2 + \dfrac{1}{4}\gamma_1\left\{\left[\left(\mu_{\boldsymbol{x}}^2 + \mu_{\boldsymbol{y}}^2\right)\left(\sigma_{\boldsymbol{x}}^2 + \sigma_{\boldsymbol{y}}^2\right)\right]^2 - \left(4\mu_{\boldsymbol{x}}\mu_{\boldsymbol{y}}\sigma_{\boldsymbol{xy}}\right)^2\right\} \\ \Phi_2 = \|\boldsymbol{d}_2 - \boldsymbol{G}_2\boldsymbol{m}_2\|_2^2 + \lambda_2\|\boldsymbol{w}_2\boldsymbol{m}_2\|_2^2 + \dfrac{1}{4}\gamma_2\left\{\left[\left(\mu_{\boldsymbol{x}}^2 + \mu_{\boldsymbol{y}}^2\right)\left(\sigma_{\boldsymbol{x}}^2 + \sigma_{\boldsymbol{y}}^2\right)\right]^2 - \left(4\mu_{\boldsymbol{x}}\mu_{\boldsymbol{y}}\sigma_{\boldsymbol{xy}}\right)^2\right\} \end{cases}, \tag{8}$$

where Φ_1 and Φ_2 represent the objective function of the gravity and vertical gradient data, respectively, $\boldsymbol{d}_1$ and $\boldsymbol{d}_2$ represent the gravity and vertical gradient data, respectively, $\boldsymbol{G}_1$ and $\boldsymbol{G}_2$ represent the forward operator of the gravity and vertical gradient data, respectively, $\boldsymbol{w}_1$ and $\boldsymbol{w}_2$ represent the weighting matrix of the gravity and vertical gradient data, respectively, λ_1 and λ_2 represent the regularized parameter of the gravity and vertical gradient data, respectively, γ_1 and γ_2 represent the weighting parameter of the gravity and vertical gradient data, respectively. Additionally, the regularized constraints [3] are adopted in this paper to effectively reduce the multiple solutions.

2.3. Local weighted SSIM joint inversion

Adding reasonable prior constraints can effectively improve the multiple solutions. The separate inverted results can constrain the joint inversion [36], and Eq. (8) can be transformed into the following equations.

$$\begin{cases} \Phi_1 = \|\boldsymbol{d}_1 - \boldsymbol{G}_1\boldsymbol{m}_1\|_2^2 + \lambda_1\|\boldsymbol{w}_1\boldsymbol{w}_{\boldsymbol{m}_2}\boldsymbol{m}_1\|_2^2 + \dfrac{1}{4}\gamma_1\left\{\left[\left(\mu_{\boldsymbol{x}}^2 + \mu_{\boldsymbol{y}}^2\right)\left(\sigma_{\boldsymbol{x}}^2 + \sigma_{\boldsymbol{y}}^2\right)\right]^2 - \left(4\mu_{\boldsymbol{x}}\mu_{\boldsymbol{y}}\sigma_{\boldsymbol{xy}}\right)^2\right\} \\ \Phi_2 = \|\boldsymbol{d}_2 - \boldsymbol{G}_2\boldsymbol{m}_2\|_2^2 + \lambda_2\|\boldsymbol{w}_2\boldsymbol{w}_{\boldsymbol{m}_1}\boldsymbol{m}_2\|_2^2 + \dfrac{1}{4}\gamma_2\left\{\left[\left(\mu_{\boldsymbol{x}}^2 + \mu_{\boldsymbol{y}}^2\right)\left(\sigma_{\boldsymbol{x}}^2 + \sigma_{\boldsymbol{y}}^2\right)\right]^2 - \left(4\mu_{\boldsymbol{x}}\mu_{\boldsymbol{y}}\sigma_{\boldsymbol{xy}}\right)^2\right\} \end{cases}, \tag{9}$$

where $\boldsymbol{w}_{\boldsymbol{m}_2}$ and $\boldsymbol{w}_{\boldsymbol{m}_1}$ is the weighting matrices of the recovered models based on the gravity vertical gradient and gravity data, respectively, and the corresponding equations as follows.

$$\boldsymbol{w}_{\boldsymbol{m}_2} = \left(\frac{|\boldsymbol{m}_2| - |\boldsymbol{m}_2|_{\min} + \varepsilon}{|\boldsymbol{m}_2|_{\max} - |\boldsymbol{m}_2|_{\min}}\right)^{-\mu_0} \tag{10}$$

In Eq. (10), let $\varepsilon = \eta^*|\boldsymbol{m}_2|_{\max}$, η is a small non-negative constant, and η is set to 0.01 in this paper. μ_0 is a small positive constant, and its general value range is $4.0 \geq \mu_0 \geq 1.0$, which is taken as 1.0 in this

paper. When $\boldsymbol{m}_1^i \le \tau_1 * |\boldsymbol{m}_2|_{\max}$, let $\boldsymbol{w}_{\boldsymbol{m}_2}^i = 1.0$, and the calculation equation in the other ranges of $\boldsymbol{w}_{\boldsymbol{m}_2}^i$ is calculated from Eq. (10). τ_1 is in the range of $(0.0, 1.0)$. Then, when $\boldsymbol{w}_{\boldsymbol{m}_2}^i \neq 1.0$, carry out normalization and get $\boldsymbol{w}_{\boldsymbol{m}_2}^i = \frac{\boldsymbol{w}_{\boldsymbol{m}_2}^i}{\boldsymbol{w}_{\boldsymbol{m}_2}^{\max}}$. Simultaneously, the calculation equation of $\boldsymbol{w}_{\boldsymbol{m}_1}$ can be displayed as following equation.

$$\boldsymbol{w}_{\boldsymbol{m}_1} = \left(\frac{|\boldsymbol{m}_1| - |\boldsymbol{m}_1|_{\min} + \varepsilon}{|\boldsymbol{m}_1|_{\max} - |\boldsymbol{m}_1|_{\min}}\right)^{-\mu_0} \tag{11}$$

For the joint inversion using the conjugate gradient method, it is necessary to calculate the gradients of the objective function shown in Eq. (9). To simplify the derivative equations, we set $\mu_{\boldsymbol{x}}$ and $\mu_{\boldsymbol{y}}$ as constants whose values depend on the reconstructed models of the previous iteration. Then, the derivatives of Φ_{SSIM} with respect to $\boldsymbol{m}_1$ and $\boldsymbol{m}_2$ can be written as the following equations.

$$\begin{cases} \dfrac{\partial \Phi_{\mathrm{SSIM}}}{\partial \boldsymbol{m}_1} = \dfrac{\partial \Phi_{\mathrm{SSIM}}}{\partial \boldsymbol{x}} \dfrac{\partial \boldsymbol{x}}{\partial \boldsymbol{m}_1} \\ = \left[\left(\mu_{\boldsymbol{x}}^2 + \mu_{\boldsymbol{y}}^2\right)^2 \left(\sigma_{\boldsymbol{x}}^2 + \sigma_{\boldsymbol{y}}^2\right) \mathrm{diag}(\boldsymbol{x} - \mu_{\boldsymbol{x}}) - 8\left(\mu_{\boldsymbol{x}}\mu_{\boldsymbol{y}}\right)^2 \sigma_{\boldsymbol{xy}} \mathrm{diag}\left(\boldsymbol{y} - \mu_{\boldsymbol{y}}\right)\right] \boldsymbol{m}_1 \\ \dfrac{\partial \Phi_{\mathrm{SSIM}}}{\partial \boldsymbol{m}_2} = \dfrac{\partial \Phi_{\mathrm{SSIM}}}{\partial \boldsymbol{y}} \dfrac{\partial \boldsymbol{y}}{\partial \boldsymbol{m}_2} \\ = \left[\left(\mu_{\boldsymbol{x}}^2 + \mu_{\boldsymbol{y}}^2\right)^2 \left(\sigma_{\boldsymbol{x}}^2 + \sigma_{\boldsymbol{y}}^2\right) \mathrm{diag}\left(\boldsymbol{y} - \mu_{\boldsymbol{y}}\right) - 8\left(\mu_{\boldsymbol{x}}\mu_{\boldsymbol{y}}\right)^2 \sigma_{\boldsymbol{xy}} \mathrm{diag}(\boldsymbol{x} - \mu_{\boldsymbol{x}})\right] \boldsymbol{m}_2 \end{cases}, \tag{12}$$

where diag () indicates the transformation of a column vector into a diagonal matrix. The derivatives shown in Eq. (12) is simple, clear, and easy to calculate. After obtaining the derivatives of the SSIM constraints, it is straightforward to solve the derivatives of the objective functions Φ_1 and Φ_2. The derivatives of the objective function Φ_1 and Φ_2 with respect to $\boldsymbol{m}_1$ and $\boldsymbol{m}_2$ can be written as following equations.

$$\begin{cases} \dfrac{\partial \Phi_1}{\partial \boldsymbol{m}_1} = \left\{ \boldsymbol{G}_1^{\mathrm{T}} \boldsymbol{G}_1 + \lambda_1 \boldsymbol{w}_1^{\mathrm{T}} \boldsymbol{w}_{\boldsymbol{m}_2}^{\mathrm{T}} \boldsymbol{w}_{\boldsymbol{m}_2} \boldsymbol{w}_1 + \dfrac{1}{4}\gamma_1 \begin{bmatrix} \left(\mu_{\boldsymbol{x}}^2 + \mu_{\boldsymbol{y}}^2\right)^2 \left(\sigma_{\boldsymbol{x}}^2 + \sigma_{\boldsymbol{y}}^2\right) \mathrm{diag}(\boldsymbol{x} - \mu_{\boldsymbol{x}}) \\ -8\left(\mu_{\boldsymbol{x}}\mu_{\boldsymbol{y}}\right)^2 \sigma_{\boldsymbol{xy}} \mathrm{diag}\left(\boldsymbol{y} - \mu_{\boldsymbol{y}}\right) \end{bmatrix} \right\} \boldsymbol{m}_1 \\ \qquad -\boldsymbol{G}_1^{\mathrm{T}} \boldsymbol{d}_1 \\ \dfrac{\partial \Phi_2}{\partial \boldsymbol{m}_2} = \left\{ \boldsymbol{G}_2^{\mathrm{T}} \boldsymbol{G}_2 + \lambda_2 \boldsymbol{w}_2^{\mathrm{T}} \boldsymbol{w}_{\boldsymbol{m}_1}^{\mathrm{T}} \boldsymbol{w}_{\boldsymbol{m}_1} \boldsymbol{w}_2 + \dfrac{1}{4}\gamma_2 \begin{bmatrix} \left(\mu_{\boldsymbol{x}}^2 + \mu_{\boldsymbol{y}}^2\right)^2 \left(\sigma_{\boldsymbol{x}}^2 + \sigma_{\boldsymbol{y}}^2\right) \mathrm{diag}\left(\boldsymbol{y} - \mu_{\boldsymbol{y}}\right) \\ -8\left(\mu_{\boldsymbol{x}}\mu_{\boldsymbol{y}}\right)^2 \sigma_{\boldsymbol{xy}} \mathrm{diag}(\boldsymbol{x} - \mu_{\boldsymbol{x}}) \end{bmatrix} \right\} \boldsymbol{m}_2 \\ \qquad -\boldsymbol{G}_2^{\mathrm{T}} \boldsymbol{d}_2 \end{cases} \tag{13}$$

Then, the conjugate gradient algorithm is adopted to solve the optimal solutions of the objective functions, and the optimal $\boldsymbol{m}_1$ and $\boldsymbol{m}_2$ can be obtained when the stopping condition is reached.

The whole process of the SSIM joint inversion with the local constraint is shown in Fig. 1, which can be divided into three steps. The first step is to use the gravity and vertical gradient data for separate inversions, and obtain the corresponding density models. The second step is to calculate the local weighting matrices according to the density models obtained from the step 1. The third step is to bring the local weighting matrix into the SSIM joint inversion framework, and the conjugate gradient method is adopted to the joint inversion. Finally, the average values of recovered density models $\boldsymbol{m}_1$ and $\boldsymbol{m}_2$ are calculated as the fused density model [36].

3. Results and validation

Synthetic data are adopted to verify the correctness of the joint inversion method mentioned above. Generally, the cross-gradient joint inversion method has been widely adopted in joint inversion for gravity and vertical gradient data. Therefore, the cross-gradient joint inversion is compared with the SSIM inversion to prove the correctness and advantages of the method developed in this paper.

3.1. Model 1

The synthetic data of model 1 covers two geological bodies shown in Fig. 2a, are utilized to verify the correctness and advantages of the SSIM joint inversion method proposed in this paper. The gravity and vertical gradient data computed from model 1 are

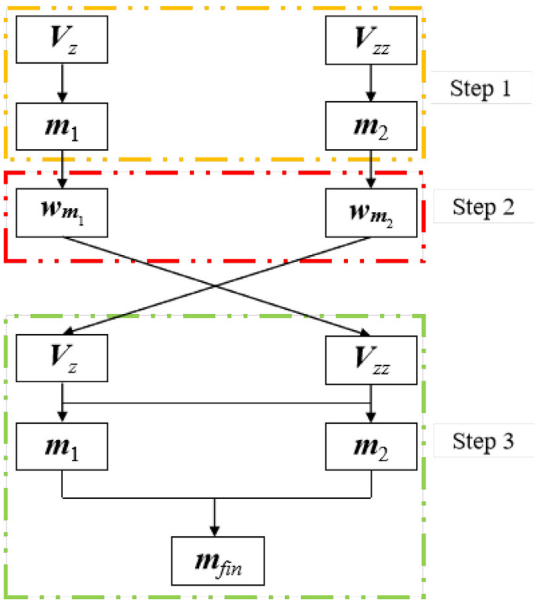

Fig. 1. The joint inversion framework with local weighting.

revealed in Fig. 2b and c, which add 2% of the maximum value of the gravity and vertical gradient data as the noises, respectively. The gravity and vertical gradient data conform to a regular grid of 20 × 20 data points, totaling 400 equally spaced data points. In the process of the inversion, there cover ten layers in depth from 0 to 1000 m, and the size of one cell is set to 100 × 100 × 100 m. From Fig. 2b and c, the horizontal resolution of the gravity gradient data is higher than that of the gravity data. The gravity data is more sensitive to the deep-density bodies than the gradient data, and the gravity gradient data is more sensitive to the shallow-density bodies.

In the inversion process of the synthetic data 1, the initial density model is set to 0.1 g/cc and the number of the iteration is set to 60. Fig. 3c and d reveal the regularized inverted results of the gravity gradient data, which presents that the vertical and horizontal resolution of the shallow geology bodies is better than that of the gravity data (Fig. 3a and b). Additionally, the resolution of deep geology bodies revealed in Fig. 3a is better than that in Fig. 3c, which verifies the data characteristics of the gravity and vertical gradient data. The reconstructed models of the regularized joint inversion using $[\boldsymbol{V}_z, \boldsymbol{V}_{zz}]^{\mathrm{T}}$ data are presented in Fig. 3e and f. Obviously, the reconstructed models of the joint inversion are better than that of the separate inversions, and the resolution of the recovered models in horizontal and vertical directions of the joint

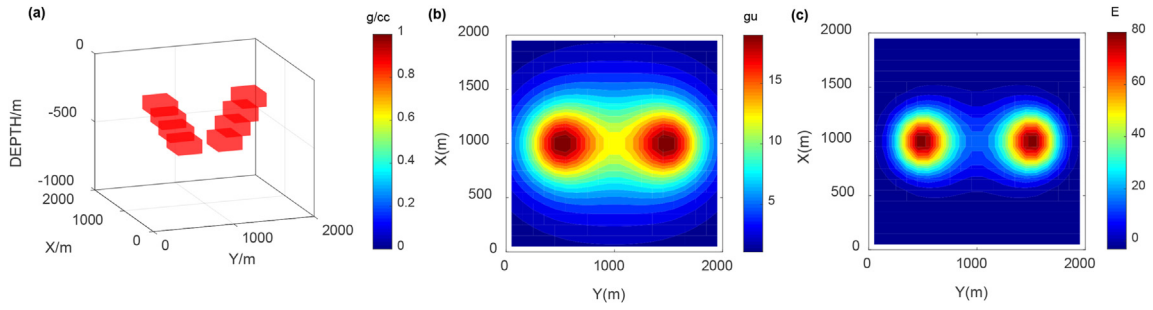

Fig. 2. (a) Spatial location of the synthetic model. The contour map of forward (b) the gravity anomaly and (c) the gravity vertical gradient data of the synthetic model 1.

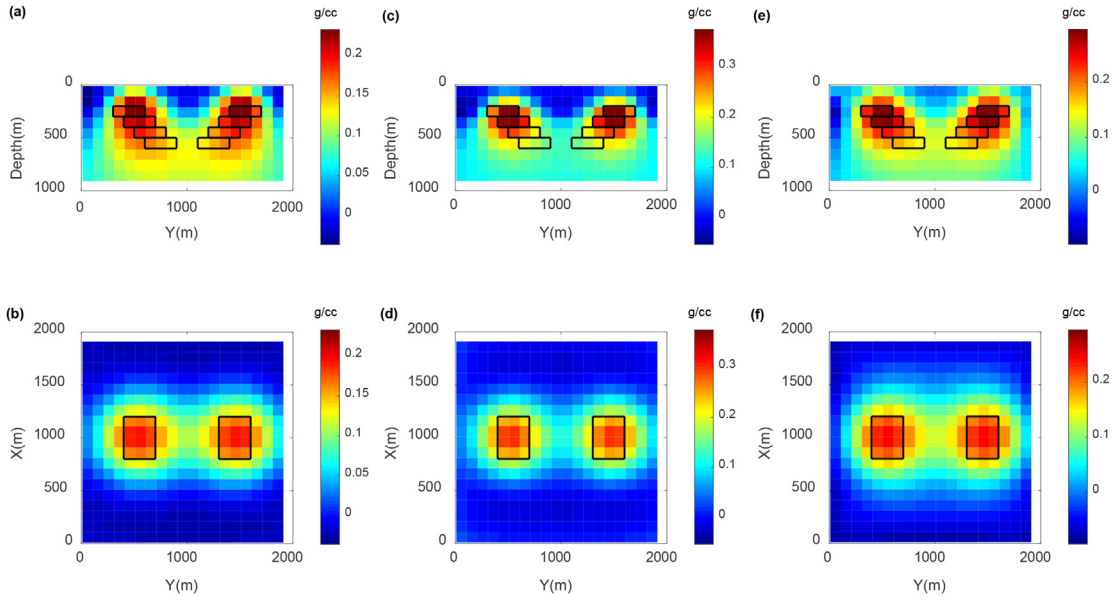

Fig. 3. The separate inversions of the synthetic data 1. (a) and (b) are the slices of the separate inversion results of the gravity data at $x = 1000$ m and $z = 400$ m, respectively. (c) and (d) are the slices of the separate inversion results of the vertical gradient data at $x = 1000$ m and $z = 400$ m, respectively. (e) and (f) are the slices of the regularized joint inversion results of the gravity and vertical gradient data at $x = 1000$ m and $z = 400$ m, respectively.

inversion is more consistent with that of the actual density models shown in Fig. 2a.

Then, the cross-gradient joint inversion is carried out for synthetic data 1, and the recovered models are presented in Fig. 4a–d the reconstructed density models are apparently focused, and the two geology anomalous bodies are better than those revealed in Fig. 3 in terms of the location and resolution.

Then, let $\gamma_1 = 2.0\times10^{11}$, $\gamma_2 = 1.0\times10^{10}$, and the SSIM joint inversion is executed. The recovered density model is displayed in Fig. 5. From Figs. 3–5, the recovered density models of the SSIM inversion are also focused, the positioning and resolution of the two geology anomalous bodies are better than that of the recovered density models shown in Figs. 3 and 4. Additionally, the resolution of the SSIM inverted results in the vertical direction is better than that of the cross-gradient inverted results, and the physical property consistency and structure consistency of the recovered results are improved.

According to the separate inversion results shown in Fig. 3, set $\tau_1 = 0.2, \tau_2 = 0.7$, and τ_2 is the parameter of the calculation matrix $\boldsymbol{w}_{\boldsymbol{m}_1}$, and set $\gamma_1 = 1.0\times10^{9}$ and $\gamma_2 = 1.0\times10^{10}$. Then, the local weighted SSIM joint inversion is carried out, and the recovered density models are displayed in Fig. 6a–d. Obviously, from Figs. 3–6, the resolution of the recovered density models of the SSIM inversion with local weighting is higher. The corresponding magnitude and distribution of physical property values of the recovered models are closer to the actual density models, which can verify the correctness and advantages of the developed method in this paper. Additionally, the fused density models are displayed in Fig. 6e and f, the gravity and vertical gradient data forward from the fused models are shown in Fig. 7a and b, and the residuals obtained from subtracting the forward and original data are displayed in Fig. 7c and d. Apparently, it can be found that the forward data of the fused density models are well consistent with the original data.

3.2. Model 2

To further certify the correctness of the proposed method, a synthetic model with inconsistent depth is utilized to verify the proposed method in this paper. The synthetic data of model 2, which also contains two geological bodies in Fig. 8a, and the gravity and gravity vertical gradient data computed from model 2 are displayed in Fig. 8b and c also add 2% of the maximum value of the corresponding gravity and vertical gradient data as the noise data, respectively. Obviously, from Fig. 8, the horizontal resolution of the gravity gradient data is higher than that of the gravity data.

The initial density model is also set to 0.1 g/cc, and the number of iterations is set to 100. Fig. 9c and d presents the regularized inverted models of the gravity gradient data, which presents that the vertical and horizontal resolution of the shallow anomalous bodies is better than the reconstructed models of the gravity data (Fig. 9a and b). Simultaneously, the resolution of the deep anomalous bodies shown in Fig. 9a is also better than that in Fig. 9c. The reconstructed models of the regularized joint inversion using $[\boldsymbol{V}_z, \boldsymbol{V}_{zz}]^{\mathrm{T}}$ data are displayed in Fig. 9e and f the resolution of the recovered models in horizontal and depth directions of the joint inversion is more consistent with that of the actual density models.

Then, the cross-gradient joint inversion method is carried out for the synthetic data 2, and the reconstructed models are displayed in Fig. 10a–10d. The recovered density models are more focused than that of the separate inversions, and the two anomalous bodies are also better than the recovered density models shown in Fig. 9 in terms of the location and the resolution.

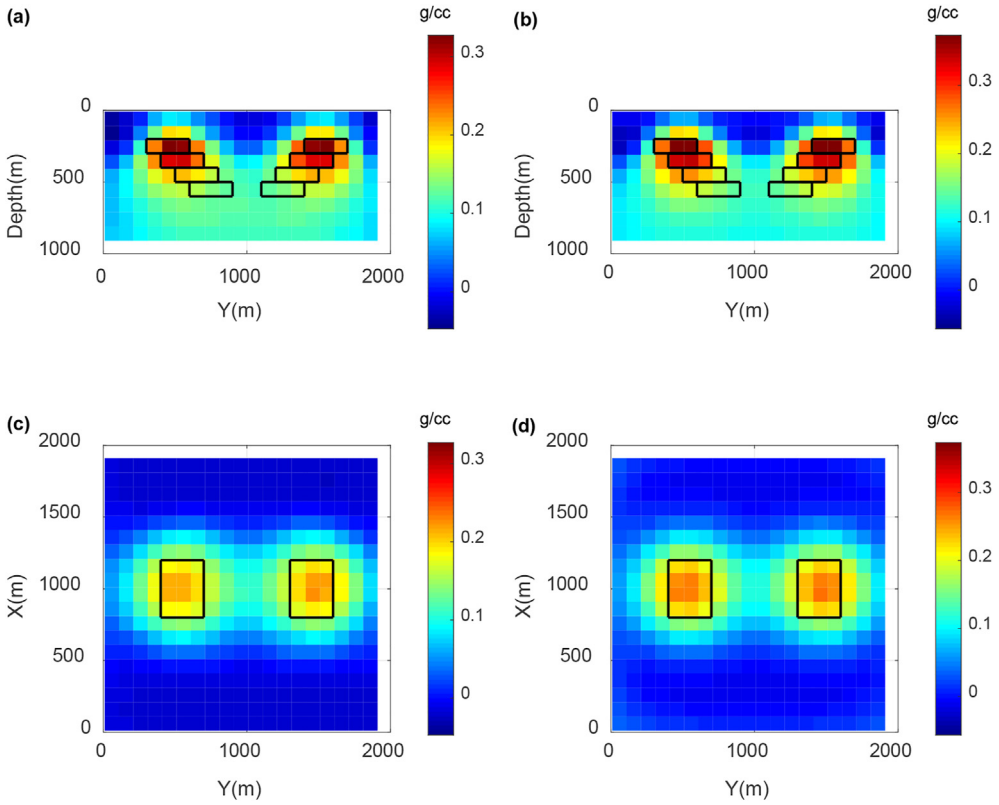

Fig. 4. The cross-gradient joint inversion of the synthetic data 1. (a) and (b) are the slices of the recovered models of the gravity data at $x = 1000$ m and $z = 400$ m, respectively. (c) and (d) are the slices of the recovered models of the vertical gradient data at $x = 1000$ m and $z = 400$ m, respectively.

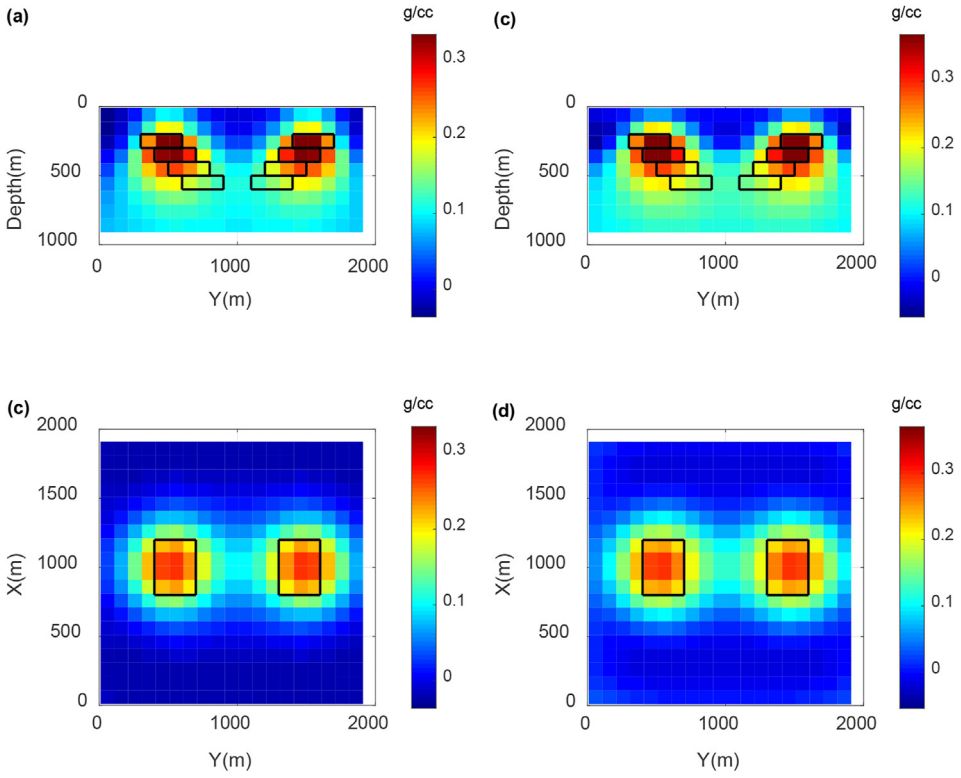

Fig. 5. The SSIM joint inversion of the synthetic data 1. (a) and (b) are the slices of the recovered models of the gravity data at $x = 1000$ m and $z = 400$ m, respectively. (c) and (d) are the slices of the recovered models of the vertical gradient data at $x = 1000$ m and $z = 400$ m, respectively.

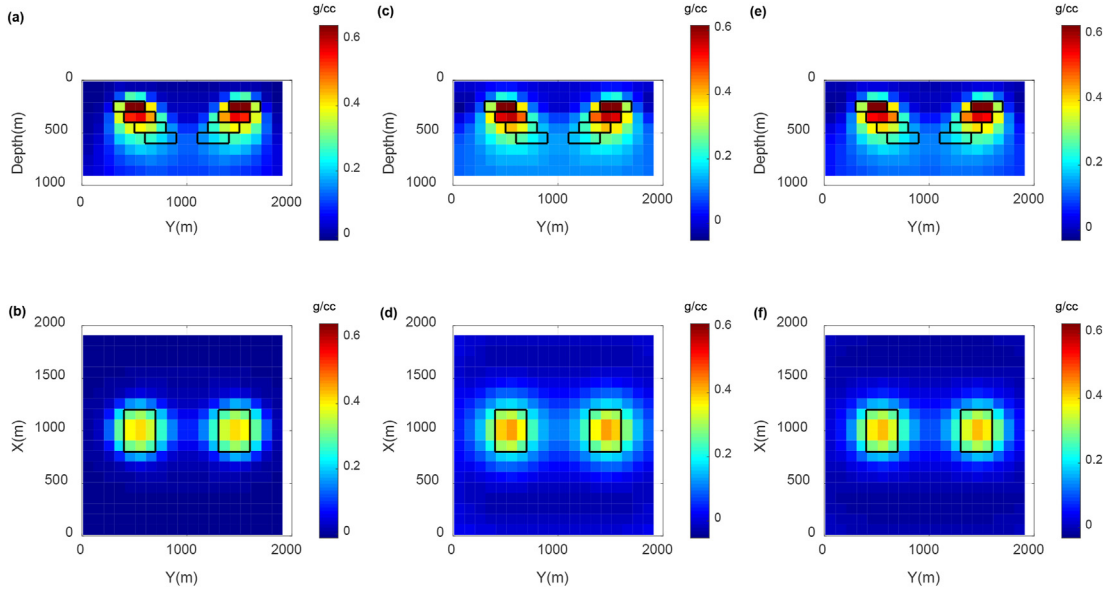

Fig. 6. The SSIM inversion based on the local weighting of the synthetic data 1. (a) and (b) are the slices of the recovered model of the gravity data at $x = 1000$ m and $z = 400$ m, respectively. (c) and (d) are the slices of the recovered model of the vertical gradient data at $x = 1000$ m and $z = 400$ m, respectively. (e) and (f) are the slices of the fused model at $x = 1000$ m and $z = 400$ m, respectively.

Then, let $\gamma_1 = 3.0\times10^{12}$, $\gamma_2 = 1.0\times10^{11}$, and the SSIM joint inversion is carried out. The recovered density models are shown in Fig. 11a–11d. From Figs. 9–11, the recovered density models of the SSIM inversion are focused, and the positioning and resolution of the two geology anomalous bodies are better than that of the recovered density models shown in Fig. 9. Additionally, the resolution of the recovered models of the SSIM joint inversion is better than that of the cross-gradient joint inversion in the vertical direction, which reveals the correctness and superiority of the method proposed in this paper.

From the separate inverted models shown in Fig. 9a–9d, set $\tau_1 = 0.2, \tau_2 = 0.7, \gamma_1 = 1.0\times10^9$ and $\gamma_2 = 5.0\times10^{11}$. Then, the local weighted SSIM joint inversion is carried out, and the recovered models are displayed in Fig. 12a–12d. Obviously, from Figs. 9–12,

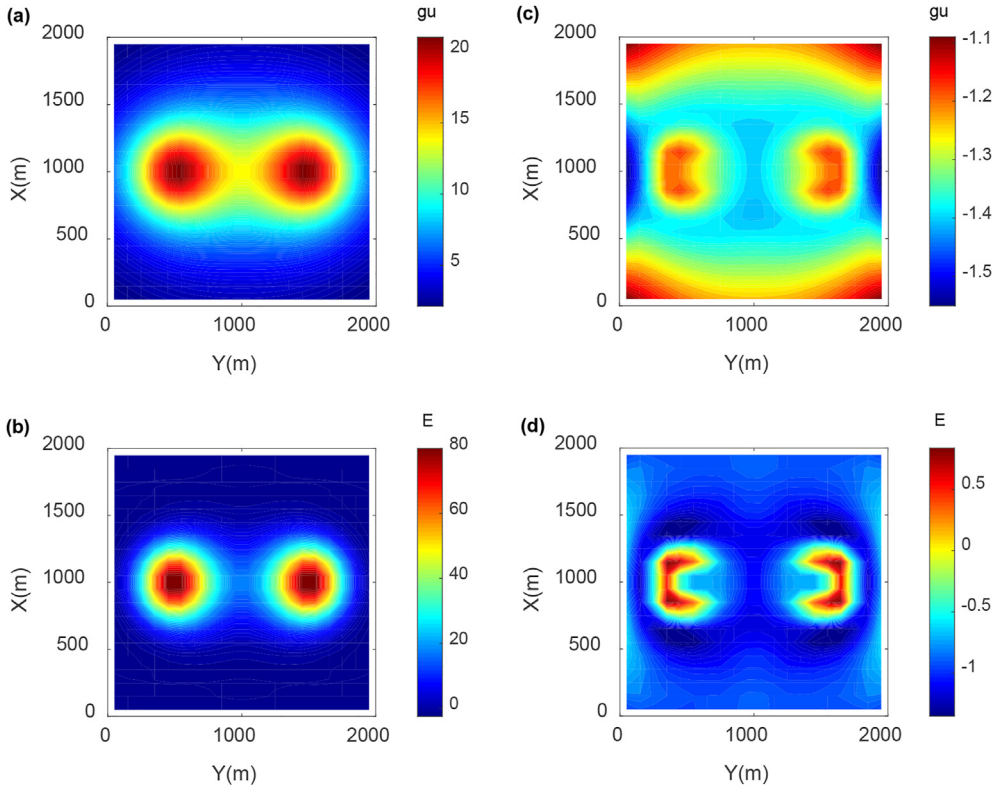

Fig. 7. The gravity data (a) and vertical gradient data (b) of the forward calculation of the fused model. (c) and (d) are the residuals of the original gravity and vertical gradient data with the forward gravity and vertical gradient data, respectively.

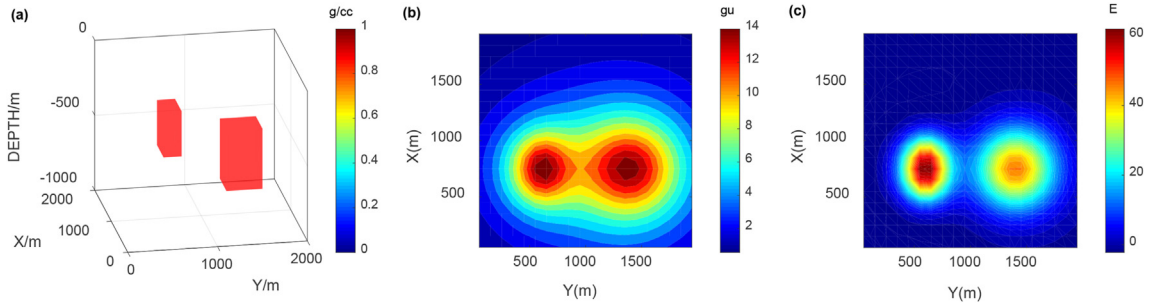

Fig. 8. (a) Spatial location of the synthetic model 2. The contour map of forward (b) gravity anomaly and (c) gravity vertical gradient data of synthetic model 2.

the resolution of the recovered models of Fig. 12 is higher than others, and the magnitude and distribution of the physical property values of the recovered density model are closer to the actual density model, which again illustrates the correctness and advantages of the proposed method in this paper. Furthermore, the fused models are shown in Fig. 12e and f, the gravity and vertical gradient data forward from the fused models are displayed in Fig. 13a and b, and the residuals are revealed in Fig. 13c and d. Apparently, the forward data is also well consistent with the synthetic data 2.

3.3. Model 3

Then, synthetic data with uneven density values and inconsistent depth is utilized for verification. The synthetic model 3 contains four geological bodies shown in Fig. 14a. The gravity and vertical gradient data computed from the synthetic model 3 are shown in Fig. 14b and c, which also add 2% of the maximum value of the corresponding gravity and vertical gradient data as the noise, respectively.

The initial density model is also set to 0.1 g/cc, and the iteration number is also set to 100. Fig. 15e–15h presents the regularized inverted models of the gravity gradient data, which displays that the vertical and horizontal resolution of the shallow anomalous bodies is better than the inverted models of the gravity data (Fig. 15a–15d).

Then, the reconstructed results of the regularized joint inversion using $[\boldsymbol{V}_z, \boldsymbol{V}_{zz}]^{\mathrm{T}}$ data are shown in Fig. 16a–16d. It can be found that the joint inversion has obvious advantages over the separate inversions in locating the depth direction of the anomalous geology bodies.

Then, the cross-gradient joint inversion method is executed for the synthetic data 3. The recovered density models of the cross-gradient joint inversion are shown in Fig. 17. From Figs. 15–17, the recovered density models shown in Fig. 17 are more focused, and the geology anomalous bodies are better than that shown in Figs. 15 and 16 in the location and resolution.

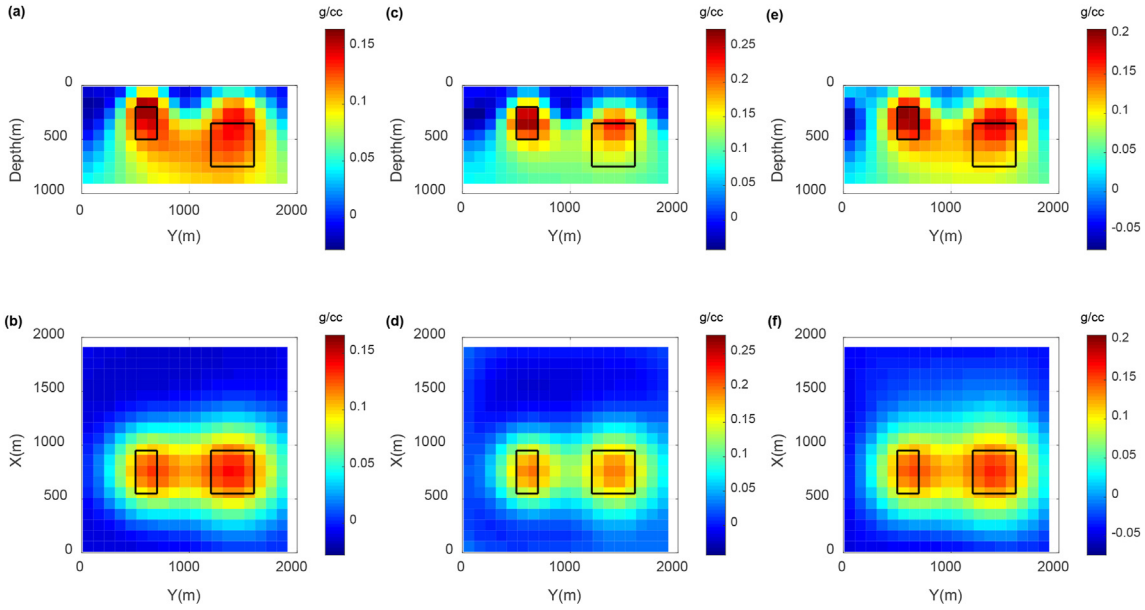

Fig. 9. The separate inversions of the synthetic data 2. (a) and (b) are the slices of the separate inversion results of the gravity data at $x = 750$ m and $z = 450$ m, respectively. (c) and (d) are the slices of the separate inversion results of the vertical gradient data at $x = 750$ m and $z = 450$ m, respectively. (e) and (f) are the slices of the regularized joint inversion results at $x = 750$ m and $z = 450$ m, respectively.

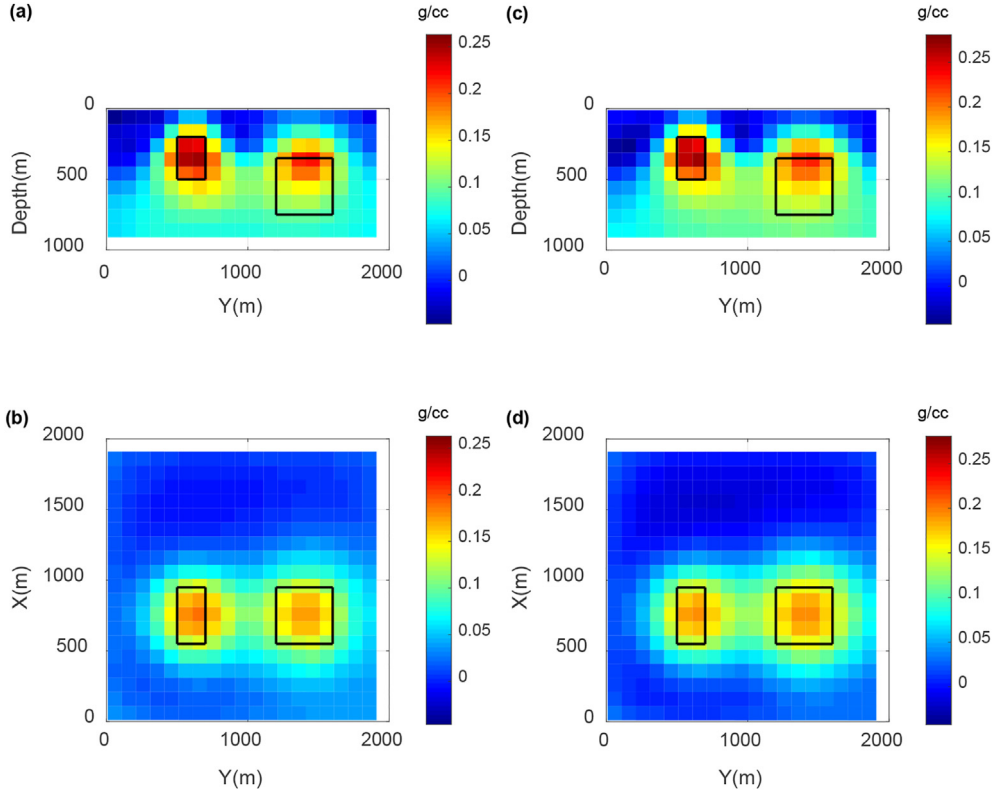

Fig. 10. The cross-gradient joint inversion of the synthetic data 2. (a) and (b) are the slices of the recovered models of the gravity data at $x = 750$ m and $z = 450$ m, respectively. (c) and (d) are the slices of the recovered models of the vertical gradient data at $x = 750$ m and $z = 450$ m, respectively.

Then, let $\gamma_1 = 2.0\times10^{11}$, $\gamma_2 = 1.0\times10^{11}$, and the SSIM joint inversion is executed. The recovered density models are shown in Fig. 18. From Figs. 15–18, the recovered density models of Fig. 18 are more focused, the positioning and resolution of the geology anomalous bodies are better than that of the recovered density models displayed in Figs. 15–17.

Then, from the separate reconstructed models, set $\tau_1 = 0.3$, $\tau_2 = 0.5$, $\gamma_1 = 1.0\times10^{10}$ and $\gamma_2 = 2.0\times10^{10}$. Then, the local weighted SSIM inversion for the synthetic data 3 is carried out, and the recovered models are displayed in Fig. 19. Obviously, from Figs. 15–19, the resolution and density contrast of the recovered density models shown in Fig. 19 is higher, and the corresponding

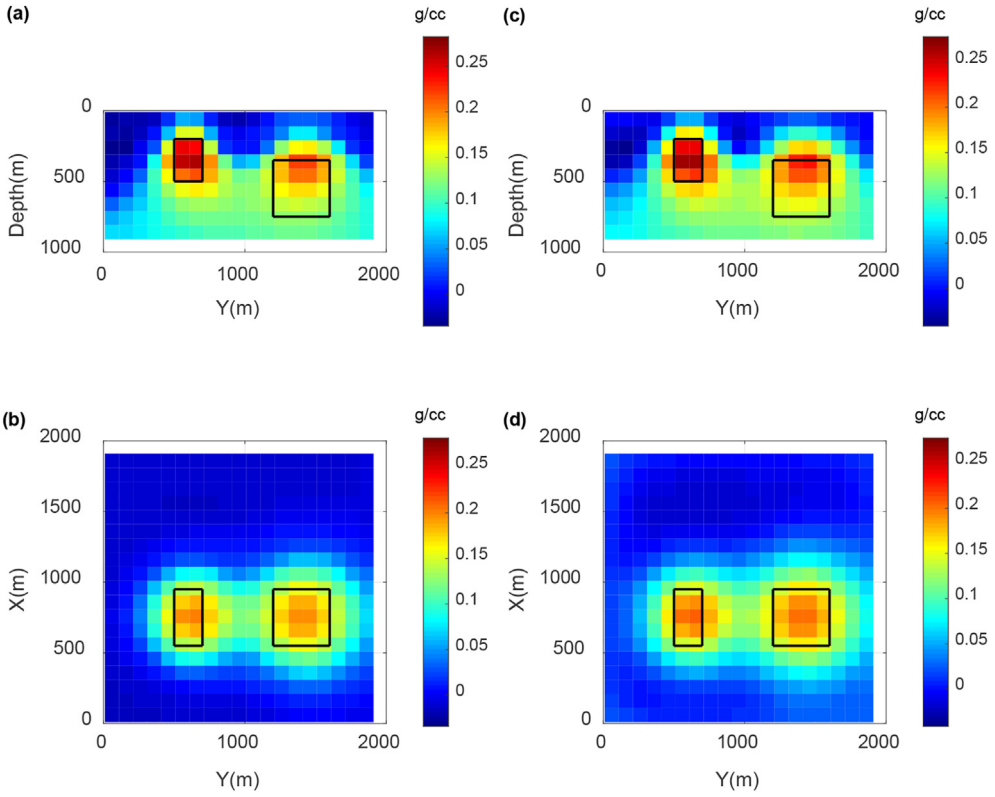

Fig. 11. The SSIM joint inversion of the synthetic data 2. (a) and (b) are the slices of the recovered models of the gravity data at $x = 750$ m and $z = 450$ m, respectively. (c) and (d) are the slices of the recovered models of the vertical gradient data at $x = 750$ m and $z = 450$ m, respectively.

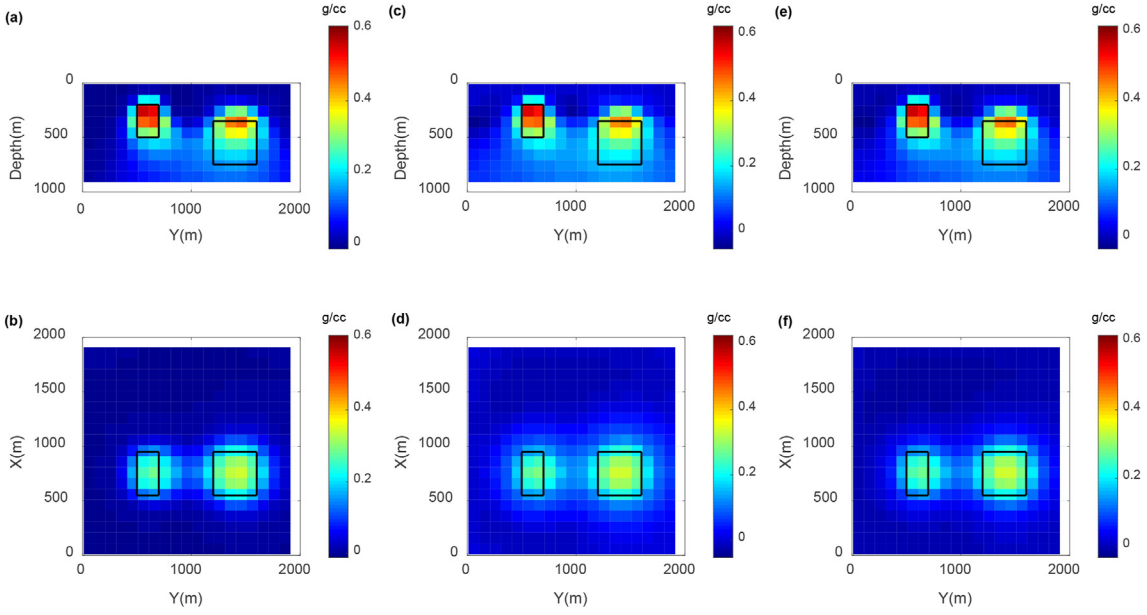

Fig. 12. The SSIM inversion based on the local weighting of the synthetic data 2. (a) and (b) are the slices of the recovered model of the gravity data at $x = 750$ m and $z = 450$ m, respectively. (c) and (d) are the slices of the recovered model of the vertical gradient data at $x = 750$ m and $z = 450$ m, respectively. (e) and (f) are the slices of the fused model at $x = 750$ m and $z = 450$ m, respectively.

magnitude and distribution of the physical property values are closer to the actual model 3, which again verifies the correctness and advantages of the developed algorithm in this paper.

Furthermore, the fused density models are presented in Fig. 20, the forward gravity and gravity vertical gradient data are displayed in Fig. 21a and 21b, respectively, and the residuals are presented in

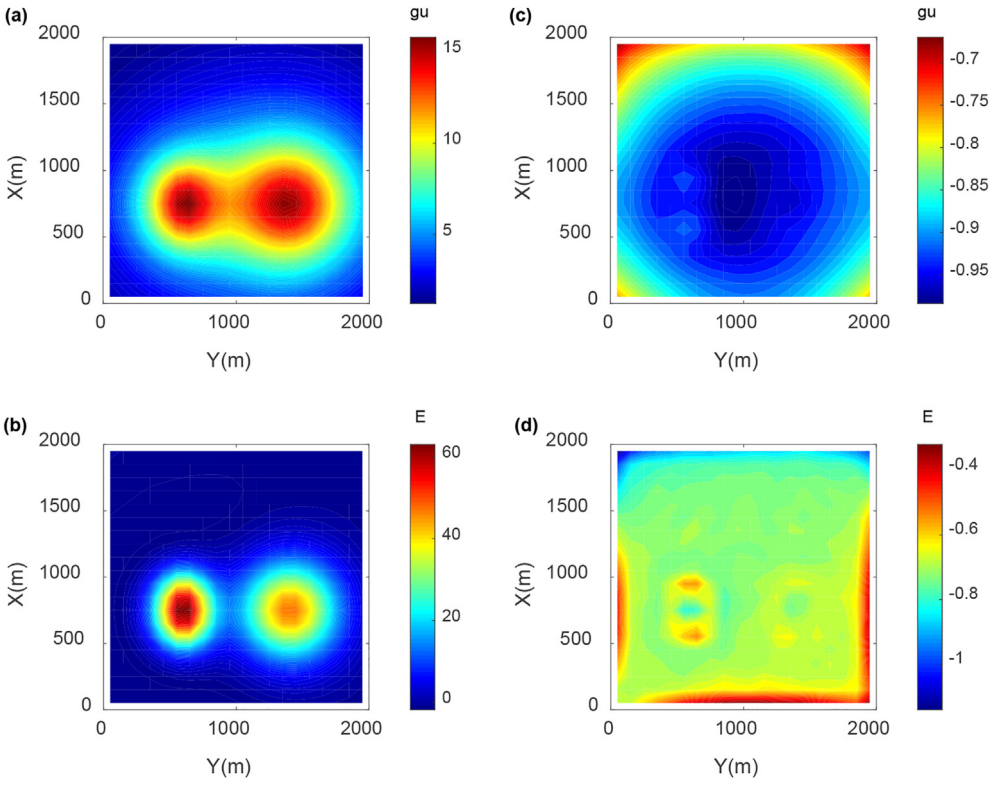

Fig. 13. The gravity data (a) and vertical gradient data (b) of the forward calculation of the fused model. (c) and (d) are the residuals of the original gravity and vertical gradient data with the forward gravity and vertical gradient data, respectively.

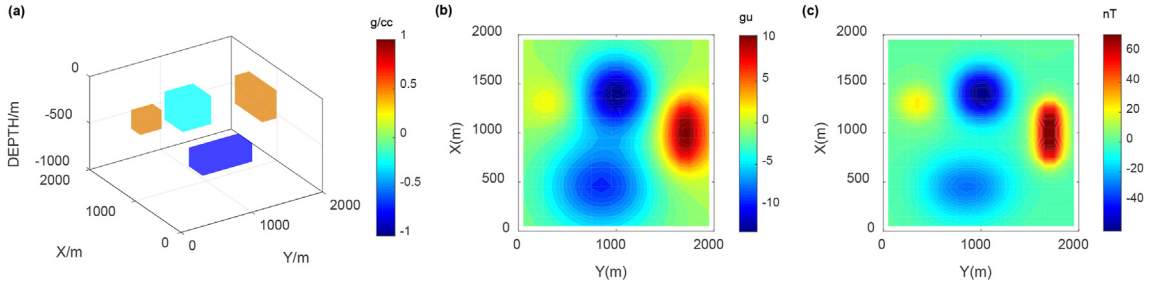

Fig. 14. (a) Spatial location of the synthetic model 3. The contour map of forward (b) gravity anomaly and (c) gravity vertical gradient data of the synthetic model 3.

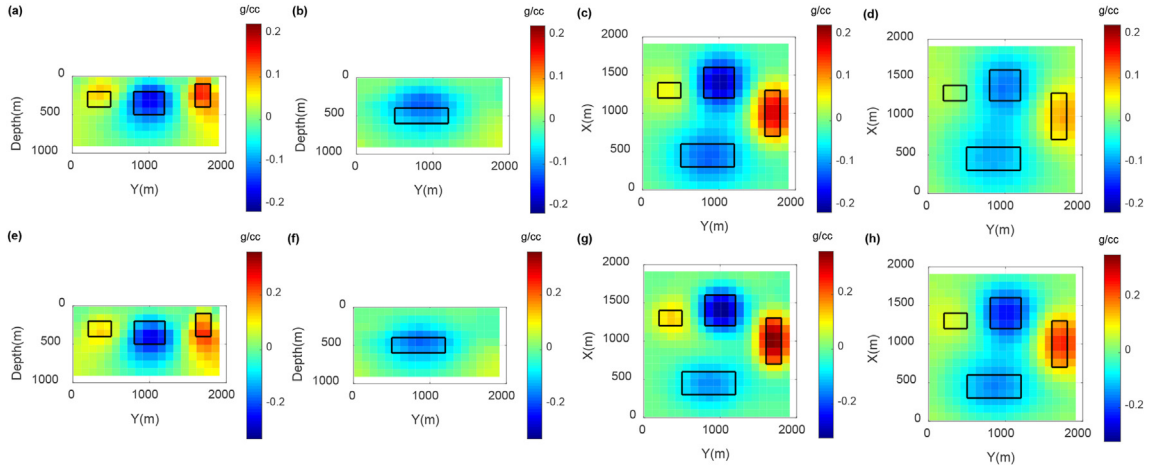

Fig. 15. The separate inversions of the synthetic data 3. (a), (b), (c) and (d) are the slices of the separate inversion results of the gravity data at $x = 1200$ m, $x = 400$ m, $z = 300$ m and $z = 500$ m, respectively. (e), (f), (g) and (h) are the slices of the separate inversion results of the vertical gradient data at $x = 1200$ m, $x = 400$ m, $z = 300$ m and $z = 500$ m, respectively.

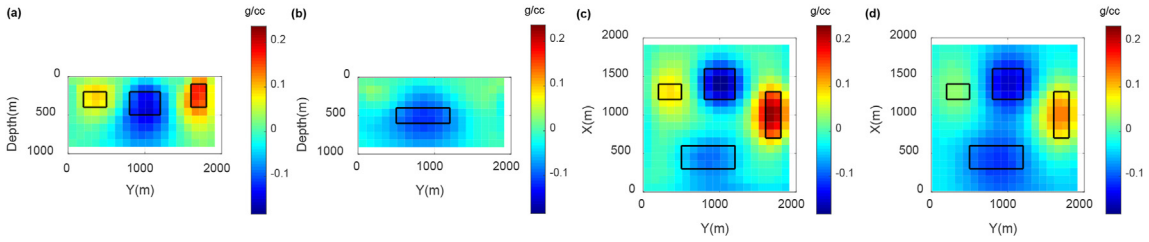

Fig. 16. The regularized joint inversions of the synthetic data 3. (a), (b), (c) and (d) are the slices of the recovered density model at $x = 1200$ m, $x = 400$ m, $z = 300$ m and $z = 500$ m, respectively.

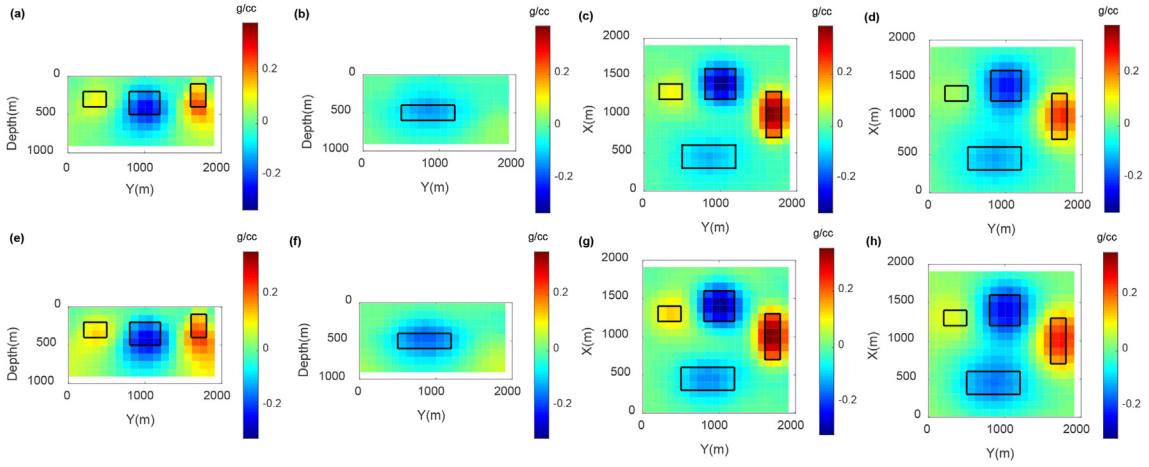

Fig. 17. The cross-gradient joint inversion of the synthetic data 3. (a), (b), (c) and (d) are the slices of the recovered model of the gravity data at $x = 1200$ m, $x = 400$ m, $z = 300$ m and $z = 500$ m, respectively. (e), (f), (g) and (h) are the slices of the recovered model of the vertical gradient data at $x = 1200$ m, $x = 400$ m, $z = 300$ m and $z = 500$ m, respectively.

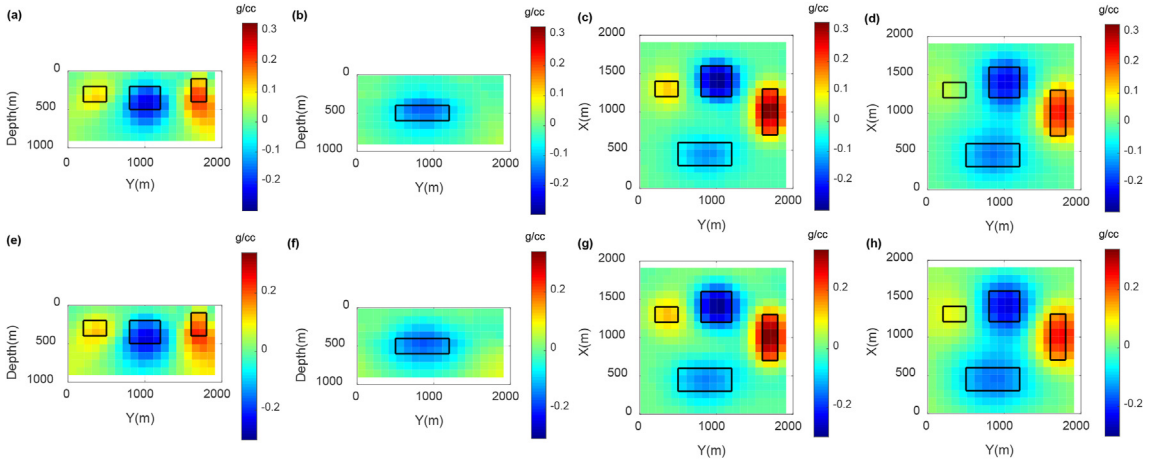

Fig. 18. The SSIM joint inversion of the synthetic data 3. (a), (b), (c) and (d) are the slices of the recovered model of the gravity data at $x = 1200$ m, $x = 400$ m, $z = 300$ m and $z = 500$ m, respectively. (e), (f), (g) and (h) are the slices of the recovered model of the vertical gradient data at $x = 1200$ m, $x = 400$ m, $z = 300$ m and $z = 500$ m, respectively.

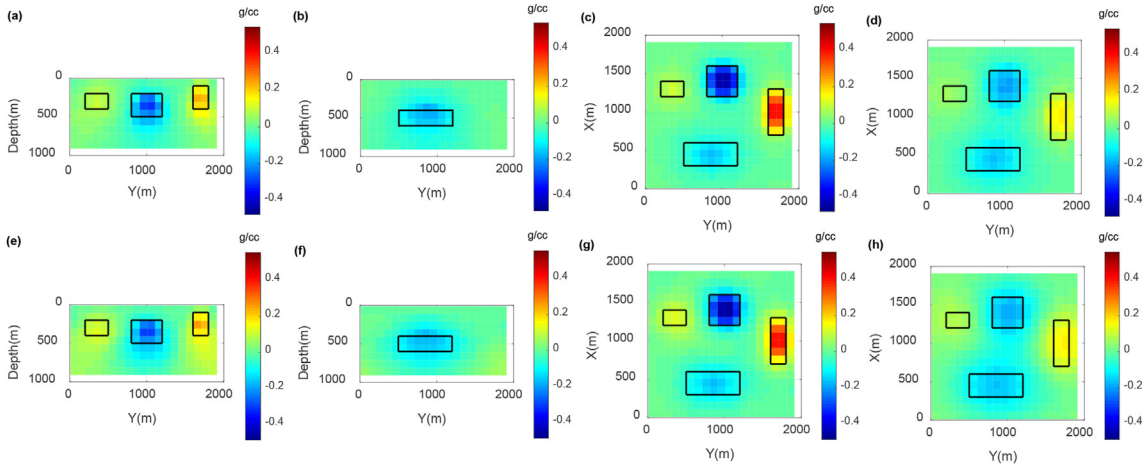

Fig. 19. The SSIM joint inversion based on the local weighting of the synthetic data 3. (a), (b), (c) and (d) are the slices of the recovered model of the gravity data at $x = 1200$ m, $x = 400$ m, $z = 300$ m and $z = 500$ m, respectively. (e), (f), (g) and (h) are the slices of the recovered model of the vertical gradient data at $x = 1200$ m, $x = 400$ m, $z = 300$ m and $z = 500$ m, respectively.

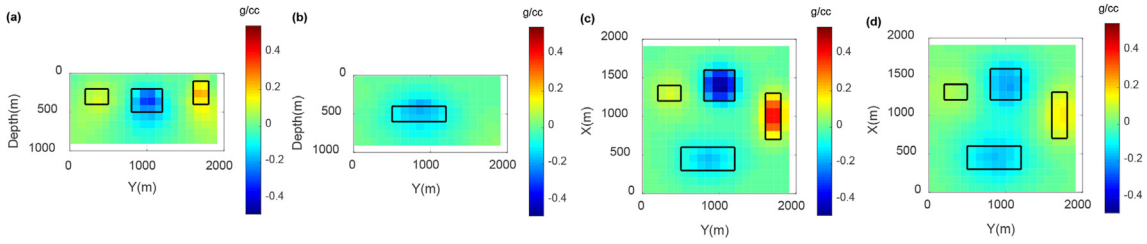

Fig. 20. (a), (b), (c) and (d) are the slices of the fused model at $x = 1200$ m, $x = 400$ m, $z = 300$ m and $z = 500$ m, respectively.

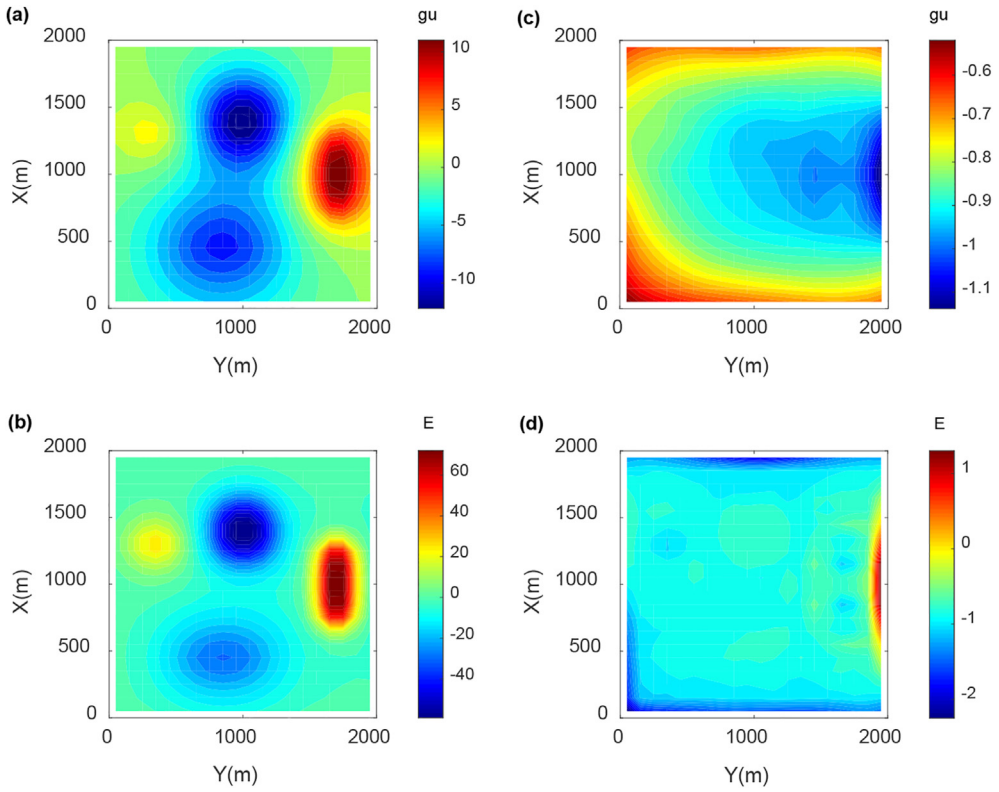

Fig. 21. The gravity data (a) and vertical gradient data (b) of the forward calculation of the fused model. (c) and (d) are the residuals of the original gravity and vertical gradient data with the forward gravity and vertical gradient data, respectively.

Fig. 21c and d. Additionally, the forward data is also consistent with the synthetic data 3.

4. Conclusions

We propose the structural and petrophysical consistency constraint based on the modified SSIM algorithm that converts the divided form to the subtracted form to avoid the emergence of the analytical singularities, which finally forms a new joint inversion method that combines the structural consistency constraint and the petrophysical consistency constraint for the gravity and vertical gradient data. Additionally, the correctness and effectiveness of the joint inversion method proposed in this paper are verified by the synthetic data, and the recovered models are much better than those of the separate inversions. Then, the synthetic data are utilized to compare the cross-gradient inversion with the SSIM inversion, and the reconstructed results have been improved by the SSIM method. Additionally, based on the separate inversion results, the SSIM joint inversion method with the local prior constraints is adopted. The corresponding recovered models present that both the locations and the density contrasts of the anomalous geology bodies are closer to the actual anomalous bodies. It can be found that the SSIM inversion method with local weight is not only a new type of joint inversion method based on the structural constraints, but also can further promote the consistency of the reconstructed results from the perspective of the values of the different physical property models, which can be considered as a more comprehensive and stronger constraint and can further reduce the non-uniqueness of the inversion. Therefore, the method proposed in this paper will be a new and efficient method of joint inversion based on the structural and petrophysical consistency constraints, which possesses good performance and high efficiency for the joint inversion and has certain application prospects in geophysical inversion.

Conflicts of interest

The authors declare that there is no conflicts of interest.

Acknowledgments

This work was supported by the National Key Research and Development Program (Grant No. 2021YFA0716100), the National Key Research and Development Program of China Project (Grant No. 2018YFC0603502), the Henan Youth Science Fund Program (Grant No. 212300410105) and the provincial key R&D and promotion special project of Henan Province (Grant No. 222102320279). Thank anonymous reviewers for their important suggestions.

References

[1] C.G. Farquharson, M.R. Ash, H.G. Miller, Geologically constrained gravity inversion for the Voisey's Bay ovoid deposit, Lead Edge 27 (1) (2008) 64–69.
[2] P.G. Lelièvre, D.W. Oldenburg, A comprehensive study of including structural orientation information in geophysical inversions, Geophys J Int 178 (2) (2009) 623–637.
[3] Y. Li, D.W. Oldenburg, Incorporating geological dip information into geophysical inversions, Geophysics 65 (1) (2000) 148–157.
[4] K.K. Afnimar, K. Nakagawa, Joint inversion of refraction and gravity data for the three-dimensional topography of a sediment-basement interface, Geophys J Int 151 (1) (2002) 243–254.
[5] M. Bosch, Lithologic tomography: from plural geophysical data to lithology estimation[J], J Geophys Res 104 (B1) (1999) 749–766.
[6] M. Bosch, J. Mc Gaughey, Joint inversion of gravity and magnetic data under lithologic constraints, Lead Edge 20 (8) (2001) 877–881.
[7] L.A. Gallardo, M.A. Meju, Characterization of heterogeneous near-surface materials by joint 2D inversion of dc resistivity and seismic data, Geophys Res Lett 30 (13) (2003).
[8] L.A. Gallardo, M.A. Meju, Joint two-dimensional DC resistivity and seismic traveltime inversion with cross-gradients constraints, J Geophys Res 109 (B3) (2004) 3311–3315.
[9] P.G. Lelièvre, C.G. Farquharson, C.A. Hurich, Joint inversion of seismic traveltimes and gravity data on unstructured grids with application to mineral exploration, Geophysics 77 (1) (2012) K1–K15.
[10] M. Moorkamp, B. Heincke, M. Jegen, et al., A framework for 3D joint inversion of MT, gravity and seismic refraction data, Geophys J Int 184 (1) (2011) 477–493.
[11] L. Guo, X. Meng, L. Shi, et al., 3D correlation imaging for gravity and gravity gradiometry data, Chin J Geophys 52 (4) (2009) 1098–1106.
[12] Z. Chen, X. Meng, L. Guo, et al., Three-dimensional fast forward modeling and the inversion strategy for large scale gravity and gravimetry data based on GPU, Chin J Geophys 55 (12) (2012) 4069–4077.
[13] M. Geng, D. Huang, Q. Yang, et al., 3D inversion of airborne gravity-gradiometry data using cokriging, Geophysics 79 (4) (2014) 37–47.
[14] P. Qin, D. Huang, Y. Yuan, et al., Integrated gravity and gravity gradient 3D inversion using the non-linear conjugate gradient, J Appl Geophys 126 (2016) 52–73.
[15] M.S. Zhdanov, W. Lin, Adaptive multinary inversion of gravity and gravity gradiometry data, Geophysics 82 (6) (2017) G101–G114.
[16] Z. Hou, D. Huang, E. Wang, et al., 3D density inversion of gravity gradieometry data with amultilevel hybrid parallel algorithm, Appl Geophys 16 (2) (2019) 141–153.
[17] L. Fu, S.X. Liu, Joint inversion of first arrival P waves and Rayleigh waves based on cross-gradient constraint, Chin J Geophys 59 (12) (2016) 4464–4472.
[18] K. Vozoff, D.L.B. Jupp, Joint inversion of geophysical data, Geophys J Int 42 (3) (1975) 977–991.
[19] G.H.F. Gardner, L.W. Gardner, A.R. Gregory, Formation velocity and density-the diagnostic basics for stratigraphic traps, Geophysics 39 (6) (1974) 770–780.
[20] L.R. Lines, A.K. Schultz, S. Treitel, Cooperative inversion of geophysical data, Geophysics 53 (1) (1988) 8–20.
[21] J. Sun, Y. Li, Multidomain petrophysically constrained inversion and geology differentiation using guided fuzzy c-means clustering, Geophysics 80 (4) (2015) ID1–ID18.
[22] J. Sun, Y. Li, Joint inversion of multiple geophysical data using guided fuzzy c-means clustering, Geophysics 81 (3) (2016) ID37–ID57.
[23] E. Haber, D. Oldenburg, Joint inversion a structural approach, Inverse Probl 13 (1997) 63–77.
[24] L.A. Gallardo, M.A. Meju, M.A. Flores-Perez, A quadratic programming approach for joint image reconstruction: mathematical and geophysical examples, Inverse Probl 21 (2) (2005) 435–452.
[25] L.A. Gallardo, Multiple cross-gradient joint inversion for geospectral imaging, Geophys Res Lett 34 (19) (2007), L19301.
[26] E. Fregoso, L.A. Gallardo, Cross-gradients joint 3D inversion with applications to gravity and magnetic data, Geophysics 74 (4) (2009) L31–L42.
[27] R. Zhang, T. Li, Joint MT and gravity inversion using structural constraints. A case study from the Linjiang copper mining area, Jilin, China, Minerals 9 (2019) 407.
[28] D.W. Oldenburg, Y. Li, Estimating depth of investigation in dc resistivity and IP surveys, Geophysics 64 (2) (1999) 403–416.
[29] C. Yin, S. Sun, X. Gao, et al., 3D joint inversion of magnetotelluric and gravity data based on local correlation constraints, Chin J Geophys 61 (1) (2018) 358–367.
[30] B. Shi, P. Yu, C. Zhao, et al., Linear correlation constrained joint inversion using squared cosine similarity of regional residual model vectors, Geophys J Int 215 (2) (2018) 1291–1307.
[31] X. Gao, S. Xiong, Z. Zeng, C. Yu, G. Zhang, S. Sun, 3D inversion modeling of joint gravity and magnetic data based on a sinusoidal correlation constraint, Appl Geophys 16 (4) (2019) 519–529.
[32] S. Liu, S. Jin, S. Xuan, X. Liu, 3D data-space joint inversion of gravity and magnetic data using a correlation-analysis constraint, Ann Geophys 65 (3) (2022).
[33] Y. Zhu, M.S. Zhdanov, M. Cuma, Gramian constraints in the joint inversion of airborne gravity gradiometry and magnetic data, SEG Technical Program Expanded Abstracts, 2013, pp. 1166–1170.
[34] M.S. Zhdanov, A. Gribenko, G. Wilson, Generalized joint inversion of multimodal geophysical data using Gramian constraints, Geophys Res Lett 39 (9) (2012).
[35] W. Lin, M.S. Zhdanov, Joint multinary inversion of gravity and magnetic data using Gramian constraints, Geophys J Int 215 (3) (2018) 1540–1557.
[36] G. Ma, X. Li, T. Wang, et al., Cross-constrained joint inversion of gravity and vertical gradient data for density structure, Chin J Geophys 65 (10) (2022b) 4111–4121.
[37] G. Ma, Y. Zhao, B. Xu, L. Li, T. Wang, High-precision joint magnetization vector inversion method of airborne vertical gradient data and gradient data with structure and data double constraints, Rem Sens 14 (10) (2022a) 2508.
[38] Q. Meng, G. Ma, T. Wang, T. Wang, High-resolution density joint inversion method of airborne and ground gravity data with cross-constraint technique, IEEE Trans Geosci Rem Sens 60 (2022) 1–9.
[39] W. Zhou, A.C. Bovik, H.R. Sheikh, et al., Image quality assessment: from error visibility to structural similarity, IEEE Trans Image Process 13 (4) (2004) 600–612.
[40] W. Zhou, A.C. Bovik, Mean squared error: love it or leave it? [J], IEEE Signal Process Mag 26 (1) (2009) 98–117.

Sheng Liu, PhD, Assistant Professor of Henan University of Urban Construction, China. His interests focused on the exploration of the interior structures of terrestrial planets using gravity and magnetic field inversion.

Xiangyun Wan, PhD, Associate professor of Henan University of Urban Construction, China. His interests focused on safety production and emergency management.

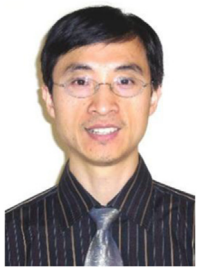

Shuangggen Jin, PhD, Professor of Shanghai Astronomical Observatory, CAS and Vice-President of Henan Polytechnic University, China. His interests focused on Satellite Navigation, Remote Sensing and Space/Planetary Exploration.